Two-dimensional polarization doping of GaN heterojunction and its potential for realizing lateral *p–n* junction devices

Zeheng Wang[1] · Liang Li[2]

Abstract

In the gallium nitride (GaN) commercial applications such as high-power illumination and portable charging station, bipolar devices are highly demanded because of their superior power transfer capability. Also, in other scenarios of the monolithic integration where high electron mobility transistors (HEMTs) or superlattice-based devices are presented, the peripheral components are preferred to be lateral. However, to realize such a lateral bipolar junction in GaN, high-concentration p-type dopant doping is still challenging and hardly compatible with the HEMT integration. In this work, we proposed a novel strategy to form lateral bipolar GaN *p–n* junctions, enabled by the two-dimensional polarization doping. The theory and the simulation reveal this strategy features inspiring forwarding, blocking, and switching performance. Given the recent success of the GaN selective area regrowth techniques, the proposed lateral bipolar junction is highly promising in monolithic heterojunction integration in the future.

Keywords Semiconductor junction · Polarization doping · Gallium nitride · Lateral device · *p–n* junction device

1 Introduction

Gallium nitride (GaN) has been reckoned as a prospective material for next-generation electron devices adopted in all kinds of applications, such as high-power illumination [1], sensing in severe conditions [2–4], wireless power transportation [5–9], and digital logic [10], thanks to its excellent material properties. In high-power applications particularly, GaN heterojunction devices are highly preferred because of the potential for realizing the monolithic integration with other components, e.g., Light Emitting Diode (LED) [11]. In these cases, the conventional GaN switching devices, e.g., High Electron Mobility Transistors (HEMTs) can sacrifice, to some extent, the chip area to obtain an enhanced Breakdown Voltage (BV) and a more increased current flow. However, within the applications requiring high-density integration, in addition to high current transportability, the small

size GaN devices are also necessary [12]. Therefore, the bipolar device architectures that can fulfill all the requirements are worth studying.

To date, some excellent innovations of GaN bipolar or bipolar-like devices have emerged [9, 13–17]. Although those designs show promising results in the current transportability, the integration of such structures suffers from incompatibility with lateral devices, limiting the further applications of such devices in the high- and low-voltage integration. Also, the realization of the highly doped p-type GaN is still a challenge [18]. These facts suggest that it is of great significance to develop a strategy to realize lateral *p–n* junctions or even bipolar devices not using dopant doping.

In this paper, we investigate a novel strategy for forming a lateral bipolar junction by utilizing the high-density carriers induced by the polarization of the GaN-based heterojunction. The proposed two-dimensional polarization doping (2DPD) scheme features bipolar current transportation and is compatible with other lateral HEMTs. We establish the fundamental theory for the 2DPD-based junction. Subsequently, we verify our strategy by experiment-calibrated simulations in which a case of novel 2DPD GaN lateral *p–n* junctions is numerically studied. As expected, the results show that the *p–n* junction owns a strong power transfer capability and a relatively high BV. Thanks to the selective area regrowth

✉ Zeheng Wang
  zenwang@outlook.com

1   School of Electrical Engineering and Telecommunications,
    The University of New South Wales, Sydney, NSW 2052,
    Australia

2   Academy for Advanced Interdisciplinary Studies, Peking
    University, Beijing 100871, China

techniques developed recently in GaN epitaxial fabrication [11, 19–24], it is more and more feasible to fabricate the proposed 2DPD *p–n* junction, rendering this scheme a promising future for GaN monolithic heterojunction integration.

2 Polarization doping strategy

In a typical Ga-plane AGaN/GaN heterojunction (A stands for Indium or Aluminum), high-density fixed charges will be induced at the upper and lower interface of the AGaN film because of the spontaneous and piezoelectric polarization [25, 26]. The polarity of the charges is determined by the lattice constant of the AGaN. Those two types of polarization charges will, respectively, attract the corresponding carriers (e.g., two-dimensional electron/hole gas, 2DEG/2DHG, for AlGaN and InGaN, respectively) at the lower interface, as schematically shown in Fig. 1. Similarly, complementary polarization charges and carriers are induced at the upper interface. As a result, it is possible to form three types of *p–n* junctions by the two-dimensional polarization: the p-i-n junction, the co-plane *p–n* junction, and the misaligned *p–n* junction, which are illustrated in Fig. 1.

2.1 Net polarization charges

Considering the polarization compensation or enhancement that comes from other mechanisms (e.g., affinity offset and Schottky barrier depletion), the net polarization charge density regarding the mole fraction *x* of the element A, which is assumed to equal the 2DEG or 2DHG density $n(x)$, can be abbreviately depicted by [25, 27, 28]:

$$n(x) = \frac{1}{e}\left[P_{\mathrm{AGaN/GaN}}(x) - U_F\left(C_{\mathrm{AGaN}} + C_{\mathrm{GaN}}\right) - Q_b\right] \tag{1}$$

where *e* is the unit charge, $P_{\mathrm{AGaN/GaN}}$ is the net polarization charge of the heterojunction, U_F is the Fermi energy of

the system, *C* is the capacitance of the material, and Q_b is the charge induced by the Schottky contact or other barrier offsets. In the case that the GaN is much thicker than the AGaN layer, the Fermi energy offset of the system could be ignored. Furthermore, if there are no other barriers presented, the net carrier density could be simplified into an expression that is only dependent on the piezo-polarization charge $P_{PZ}(x)$ and the spontaneous polarization charge $P_{SP}(x)$ [29]:

$$n(x) = \frac{1}{e}P_{\mathrm{AGaN/GaN}}(x) = \frac{1}{e}\left[P_{PZ}(x) + P_{SP}(x)\right] \tag{2}$$

In the AlGaN/GaN and InGaN/GaN heterojunction for instance, given the typical mole fraction *x* and thickness of the materials, e.g., $0.1 \leq x \leq 0.6$ and AGaN thickness > 10 nm, the carrier density can be further simplified by polynomial fitting, resulting in

$$n_{\mathrm{Al}}(x) = \frac{1}{e}\left(1.9x^2 + 2.0x\right) \times 10^{-6}\,\mathrm{cm}^{-2} \tag{3}$$

And

$$n_{\mathrm{In}}(x) = \frac{1}{e}\left(4.9x^2 + 13.8x\right) \times 10^{-6}\,\mathrm{cm}^{-2} \tag{4}$$

respectively. In realistic, taking into account the polarization attenuation caused by the charged traps or surface/interface defects, a linear scaling factor should be multiplied by the carrier charge density, such as:

$$n'(x) = \gamma^F \cdot n(x) \tag{5}$$

where γ is the attenuation factor which is usually 0.2 according to the experiments [30], and *F* is for further fitting (to simplify, we adopt $F = 1$ here). Note that the γ has already included the influence of the Fermi–Dirac distribution of the traps regarding the trap energy level. As a result, the net carrier density versus the Mole fraction of the A element can be drawn in Fig. 2, where the AlGaN or InGaN layers are assumed to be fully strained by the GaN substrate. It is clear that the 2DPD-based carriers feature a high sheet density which enables a low series resistance and, therefore, a high-power transfer capability. It should also be noted that according to Fig. 2, it is impossible to form a balanced *p–n* junction using an individual Mole fraction. Instead, different Mole fractions should be adopted in the AlGaN and InGaN layers to achieve the matched carrier density.

2.2 Turn-on voltage

Three typical 2DPD junctions can be formed in the AGaN–GaN heterojunction systems, using 2DEG (2DHG) induced above (beneath) the AGaN layer (or vice versa, depending on A's choice) by electrically contacting the 2DHG and 2DEG, as shown in Fig. 1. There will be a barrier for both carriers in the unintentionally doped AGaN
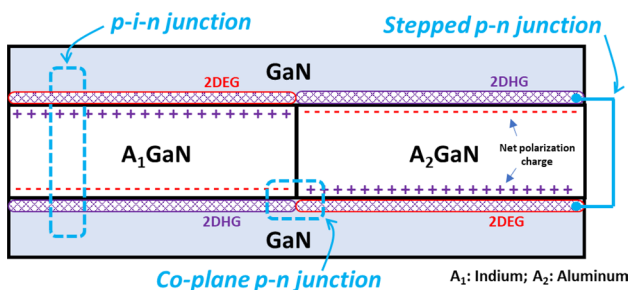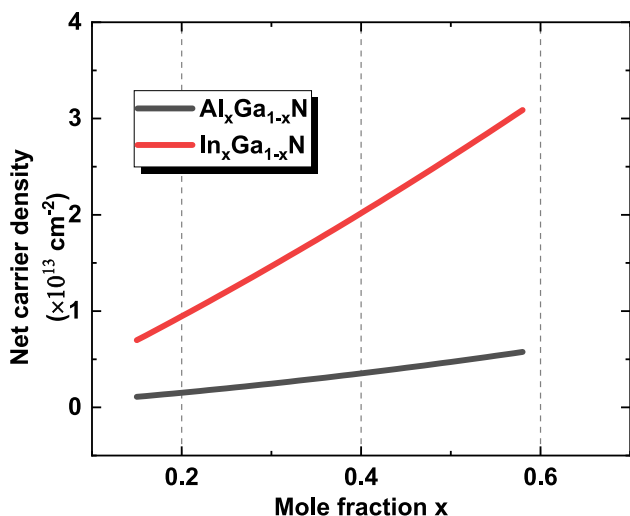

Fig. 1 The strategy of two-dimensional polarization doping where three typical architectures of the *p–n* junction using such polarization doping technique are presented. Depending on the requirement of the orientation of the net polarization, the trinary material could be InGaN or AlGaN

Fig. 2 The two-dimensional net carrier density from the polarization doping

because the AGaN consistently exhibits a larger bandgap or a high conduction and valance band offset. Consequently, the p-i-n junction is less preferred in general applications due to the limited current transport capability. Thus, using two different types of AGaN layers, a more realistic p–n junction could be formed on the GaN plane. Otherwise, using only the AGaN layer could also create the p–n junction—it requires a misalignment or a step for the two homogenous AGaN layers to match the 2DHG to the 2DEG.

For example, if aligning an $In_{x1}Ga_{1-x1}N$ layer and an $Al_{x2}Ga_{1-x2}N$ layer on the GaN, a lateral p–n junction will be formed laterally along the inhomogeneous heterojunctions with a turn-on voltage V_{bi} where

$$V_{bi} = V_{temp} \cdot \ln\left(\frac{n_{In}(x_1) \cdot n_{Al}(x_2)}{n_{i,GaN}^2}\right) \tag{6}$$

Here, V_{temp} is the baseline voltage determined by the environment temperature (e.g., 26 mV in room temperature) [31], and V_{bi} can be considered a voltage that is scaled from the baseline voltage regarding the junction's induced and intrinsic charge density. We employ 1×10^{-15} cm^{-2} as the intrinsic carrier density of the GaN $n_{i,GaN}$ [32]. The relationship between the Mole fraction x and V_{bi} can then be plotted in Fig. 3a. It suggests from the figure that the turn-on voltage of the proposed 2DPD-based junction is around 3.3 V and is stable enough to be immune from the variation of the fabrication process.

2.3 Breakdown voltage

Besides, considering the 2DHG and the 2DEG are laterally aligned (the AGaN layers may have misalignment). From the Poisson equation, it is straightforward to obtain the depletion region width W of the 2DPD junction:

$$W = \sqrt{\frac{2\epsilon_{GaN}(V_{bi}+V_R)}{e}\left(\frac{n_{In}(x_1)+n_{Al}(x_2)}{n_{In}(x_1) \cdot n_{Al}(x_2)}\right)} \tag{7}$$

together with the peak electric field E_{peak} in the junction:

$$E_{peak} = \frac{-2(V_{bi}+V_R)}{W} \tag{8}$$

where ϵ_{GaN} and V_R are the dielectric constant, and the reverse bias applied to the junction, respectively. Provided $BV \gg V_{bi}$ at the breakdown, the BV is then to be the V_R
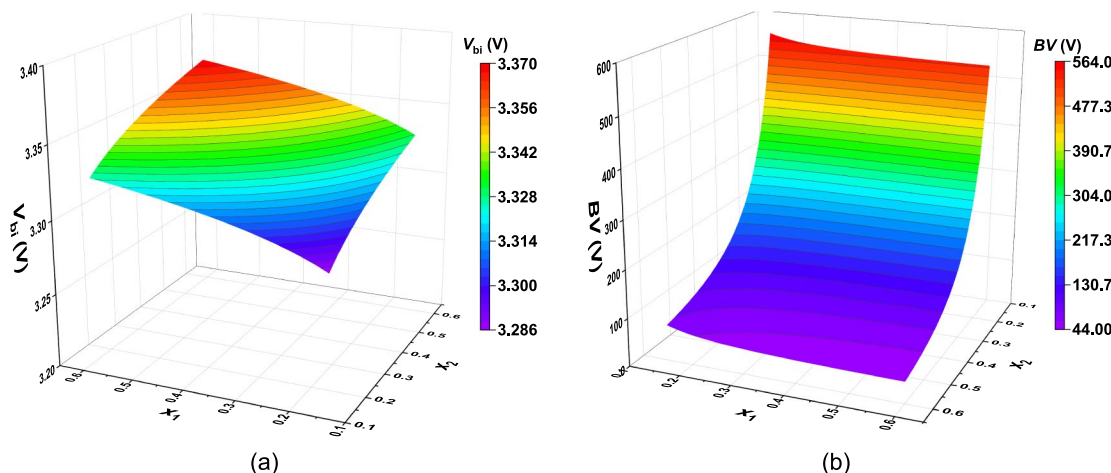

(a)

(b)

Fig. 3 a The theoretical turn-on voltage of the two-dimensional polarization doping-based inhomogeneous lateral p–n junction regarding the mole fraction of element A in the AGaN layer. **b** The

theoretical breakdown voltage of the two-dimensional polarization doping-based inhomogeneous lateral p–n junction regarding the mole fraction of element A in the AGaN layer

when the electric field reaches the critical electric field E_C [33] and can be given by:

$$BV(x_1, x_2) = \frac{\epsilon_{GaN} E_C^2 N_0(x_1, x_2)}{2e} \qquad (9)$$

where

$$N_0 = \frac{n_{In}(x_1) + n_{Al}(x_2)}{n_{In}(x_1) \cdot n_{Al}(x_2)} \qquad (10)$$

and $\epsilon_{GaN} = 8.4 \times 10^{-13}$ F/cm. Then, the $BV(x_1, x_2)$ can be plotted in Fig. 3b versus the Mole fractions. Note that in Fig. 3b, the BV is determined by the Mole fraction of the AlGaN layer, which is because compared to the charge density induced by the InGaN, the AlGaN generates fewer charges with the same mole fraction. This can also be deducted from the net carrier density in Fig. 1, where at the lower interface if the Mole fractions are the same, the AlGaN–InGaN junction is a $n^- p^+$ junction.

From the analysis above, the 2DPD-based p–n junction is preferred to be introduced into high-power applications, particularly those requiring lateral small-size monolithic integration. In the next section, we will carry out an experiment-calibrated simulation exploring the potential of realizing high-performance bipolar devices to verify this.

3 Verification and discussion

As shown in Fig. 4a, we adopt the stepped AlGaN–AlGaN junction with the same Mole fraction for the example, where the two quantum wells are aligned to each other horizontally. This aligned quantum well could allow the 2DEG and the 2DHG to diffuse to each other's region, leaving the polarization charges unmoved as the space charge. In this paper, we

introduce a parameter, misalignment, in the simulation to evaluate the variation from the fabrication process, shown in Fig. 4a. For the DC simulation, the SDevice tool from Sentaurus TCAD was adopted to achieve a more accurate solution and clearer exhibitions of the physical variables. The calibrated Sentaurus simulator was adopted from our previous work [34]. However, in order to achieve a better convergence in breakdown simulation, the Silvaco was used in this work. The calibration was also carried out for the Silvaco simulator, as shown in Fig. 4a: Firstly, a lateral bipolar GaN heterojunction device structure (a p-GaN gate HEMT) that is exactly the same as the fabricated one was established in the software to calibrate the simulation tool. The simulated transfer curves were then fitted against experiment results from ref [35]. Except for the traps and polarization relaxation settings that were modified to fit the experiment results, other material parameters were directly adopted from the built-in database of Sentaurus and Silvaco-TCAD [36]. As shown in Fig. 4a, the simulation curves fit well with the experiment, indicating reasonable simulation settings. After the calibration, a device sample, with the structure shown in Fig. 4b, was then introduced into the simulators. A 100-nm Si_3N_4 layer for passivation was also included on the device surface for an even higher reality.

The energy band structure near the interface of the simulated device at the off state is shown in Fig. 5. The heterojunctions with proper barriers and wells are clearly formed. A slight background doping (1×10^{10} cm^{-3} for both minorities and majorities) was introduced in the simulation for the convergence enhancement. As a result, there appears small energy offset between the n-type and the p-type regions. Figure 5 suggests that in a near-ideal case, the 2DPD scheme is feasible in such a heterojunction system, regardless of the slight background impurities.
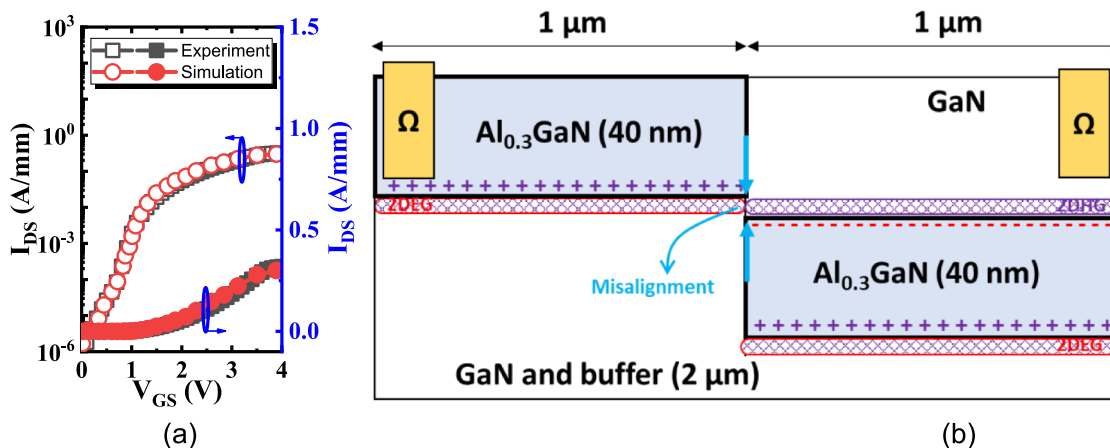

Fig. 4 The structure of the simulated GaN gas p–n junction. **a** The simulation tools are calibrated with the experiment results and **b** the schematic cross section of the device
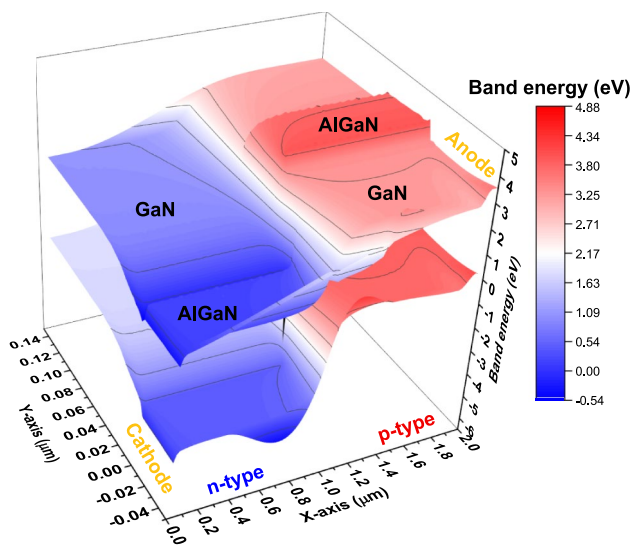
Fig. 5 The 3D band diagram of the simulated device in the off state (initial charge-balanced status). The offset between the n-type and the p-type regions comes from the slight background doping for the convergency enhancement (1×10^{10} cm^{-3} for both minorities and majorities)

The simulated current–voltage (*I–V*) curves are shown in Fig. 6a, b, where more than 350 A/mm forward current is achieved when the forward bias is 4 V, denoting the high-performance transportation of the proposed 2DPD junction, as expected. Also, a simulated turn-on voltage of 3.3 V matches the theoretical analysis, labeled in the same

figure. Moreover, with a misalignment of up to 20 nm between two quantum wells (misalignment is illustrated in Fig. 4b, the *I–V* curves are almost unchanged, suggesting this design has a good margin to allow the errors introduced from the fabrication process. The changes in the carrier densities and the energy band structures along the lateral 2DHG-2DEG channel are shown in Fig. 6c, where the lateral 2DHG-2DEG junction exhibits typical behaviors of the *p–n* junction, and the width of the depletion region matches the theoretical modeling as well, as expected in the theoretical analysis.

When the misalignment is negative, the main 2DHG-2DEG channel is cut off, resulting in a severely degraded forward current (below 100A/mm, one-fifth of the current through the main channel, see Fig. 6a), where the current is mainly contributed by the vertical p-i-n junction transportation (see Fig. 7a, b). Comparing the current curves in Fig. 6b, one can deduce that the p-i-n junction slightly turns on only after the turn-on of the main channel. The detailed evidence is provided by the simulation, as shown in Fig. 7c, d, where two main conducting paths can be observed in the simulation. The main channel is the low-resistance 2DHG-2DEG channel (the co-plane *p–n* junction); the other transport channel is the vertical GaN–AlGaN–GaN junction (the *p-i-n* junction). Considering Figs. 6 and 7, once the channel is off because of the misalignment, the transport capability of the 2DPD device will be dramatically decreased, suggesting that a positive misalignment is much more preferred in the fabrication.
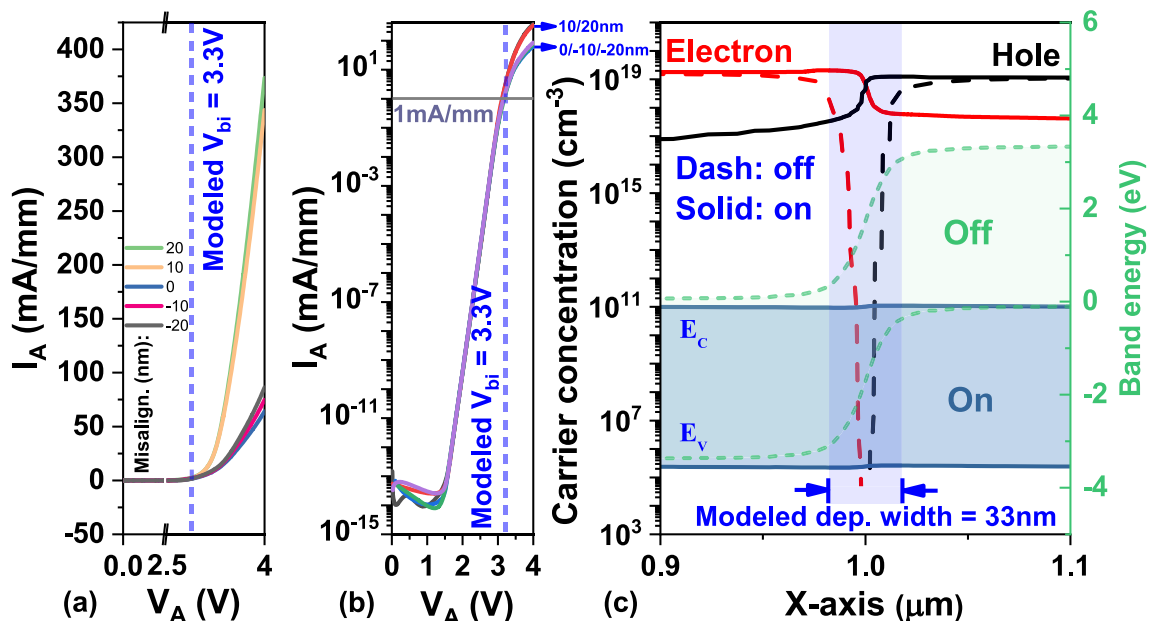

Fig. 6 The simulation results of the AlGaN–AlGaN (*x* = 0.3) junction. **a** The *I–V* curves of the junction. **b** The *I–V* curves in semi-log scale. **c** The band structure of the junction (in green) near the lateral 2DHG-2DEG interface and the carriers' distribution along the channel, at the off (initial) and the on-state
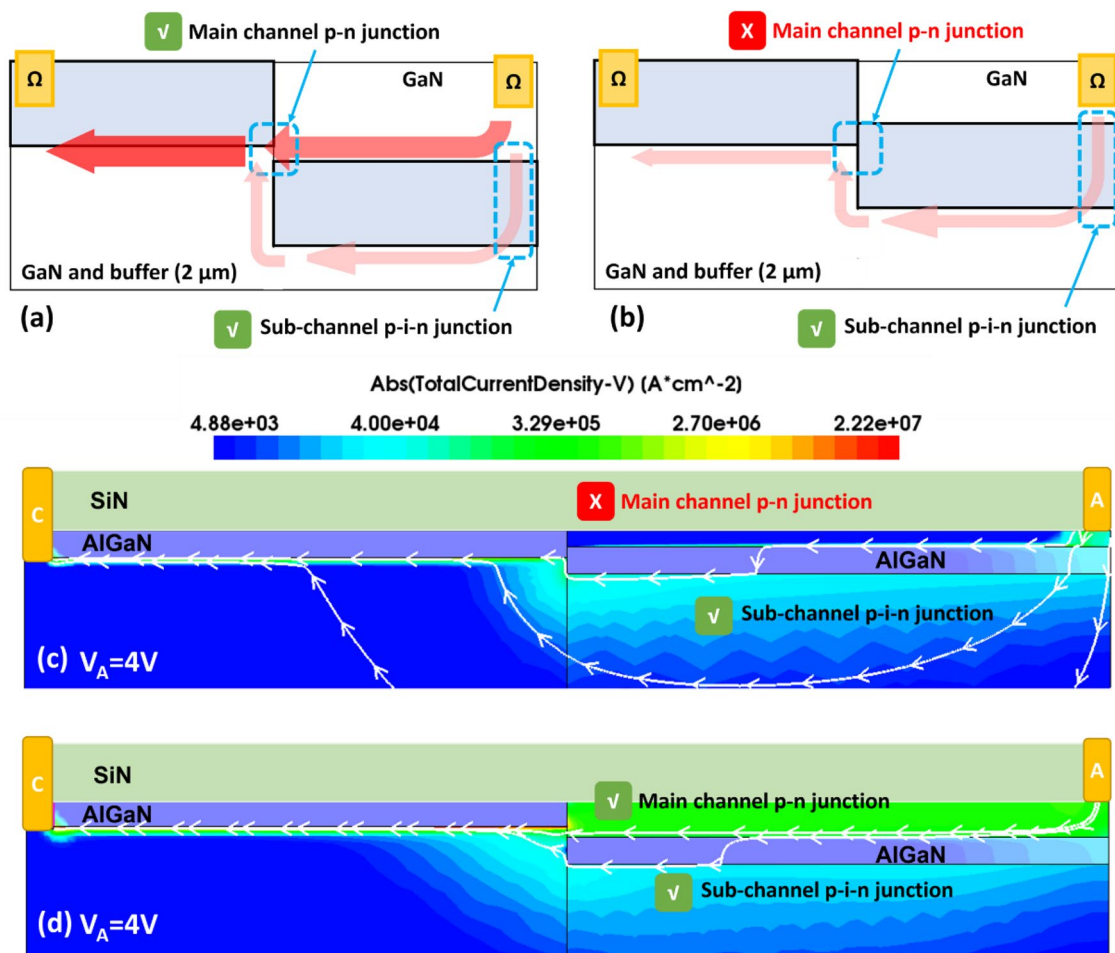
Fig. 7 The current transport mechanisms of the simulated device in the **a** positive misalignment and **b** negative misalignment conditions. The **c** and **d** are the simulated current density distribution and the corresponding current streamflow (first several strongest lines) in the two types of devices. Two main conducting paths are observed in the simulation: one is the main channel conduction, which is through the low-resistance 2DHG-2DEG channel (the co-plane *p–n* junction) that will be pinched at off state; the other transport path is through the vertical GaN–AlGaN–GaN junction (the *p*-i-*n* junction) that can contribute to a certain degree of the current transport, depending on the device design

Figure 8 shows the carrier distribution of the simulated device at the on and off state. This figure is another piece of evidence that the proposed 2DPD device features the typical behaviors of *p–n* junctions and holds higher performance due to the high-concentration carrier gases. As shown in Fig. 8a, c, the minorities can be successfully injected through the 2DHG-2DEG junction, and the majorities can be induced by the high-density carrier injection. Compared to the off state (see Fig. 8b, d), the excess carriers can extinct quickly in the switching mode through the 2D channel, where the carriers feature high mobility. Note that in order to clearly illustrate the functionality of the lateral 2DHG-2DEG junction, the polarization charges under the AlGaN in the p-type region were shadowed. Those positive charges may also induce 2DEG that can contribute to the current transport in the sub-channel but as discussed above this influence is not dominant.

Figure 9a shows the simulated BV curves of the junction. With a total length of 2 μm, the samples with three different misalignments all feature a BV of more than 200 V. The larger misalignment slightly increases the BV because the larger misalignment equivalently introduces a longer undoped region between 2DHG and 2DEG. This undoped region could be referred to as an unintentionally doped region as in conventional devices, which would flatten the electric field peak and enhance the blocking capability. Similarly, the theoretically modeled BV is labeled in the inset, demonstrating that the simulated results are consistent with the theory. However, it should be noted that when the misalignment is negative, the p-type quantum well is higher than the n-type well, and therefore the device can only provide a limited current transport in forwarding bias. It is not significant to discuss the BV performance of such devices.
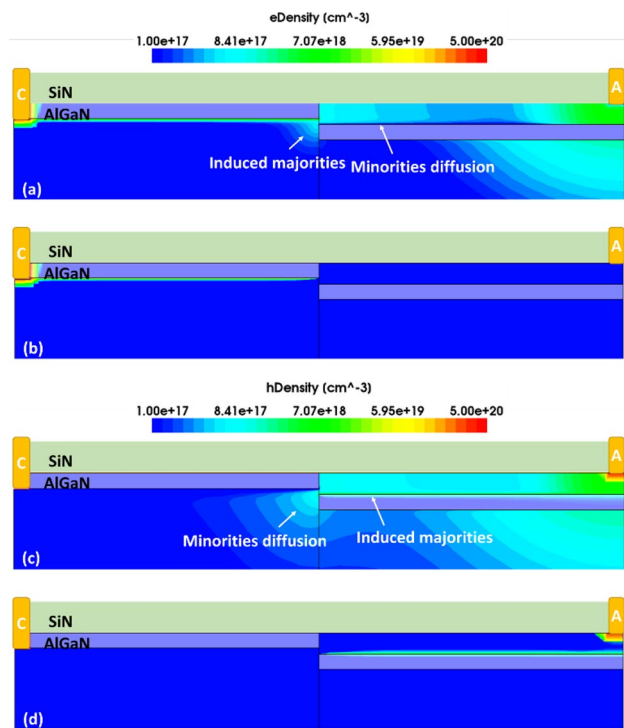
Fig. 8 The **a/b** electrons and **c/d** holes distribution at (**a**)/(**c**) on ($V_A = 4$ V) and (**b**)/(**d**) off state ($V_A = 0$ V). The overwhelming injection and the consequent majorities induction can be observed in both n- and p-type regions. Also, the evidence of minorities injection is clear for both electrons and holes, as in (**a**) and (**c**). In order to clearly illustrate the functionality of the lateral 2DHG-2DEG junction, the polarization charges under the AlGaN in the p-type region were shadowed. Note that those positive charges may also induce 2DEG that can contribute to the current transport in the sub-channel

In addition to the direct-current analysis, we also simulate alternating-current. As in Fig. 9b, which shows the reverse recovery curves of the junction, when the input voltage is switched from 5 to -20 V, the reverse peak current $I_{rr} = 0.2$ A and the recovery time $t_{rr} = 3.7$ ns, which are similar to the recent results of the experimental GaN device and are highly competitive with the Silicon counterparts [37]. This achievement is owing to the high mobility of the 2DEG and 2DHG. Furthermore, it can be suggested that the high equivalent doping concentration in this junction suppresses the minor carrier and shortens the space charge region, resulting in a low junction capacitance and, therefore, an excellent high-frequency performance.

However, in reality, when two vertical heterojunctions contact laterally, as in the example shown in Fig. 4b, two lateral AlGaN–GaN junctions (mismatch in c-plane) will be also formed. This indeed will bring extra polarizations into the system in the sense of reducing the polarization strength of two vertical heterojunctions around the central region. Consequently, the real current channel will be an unintentional p-i-n junction. The disadvantage of
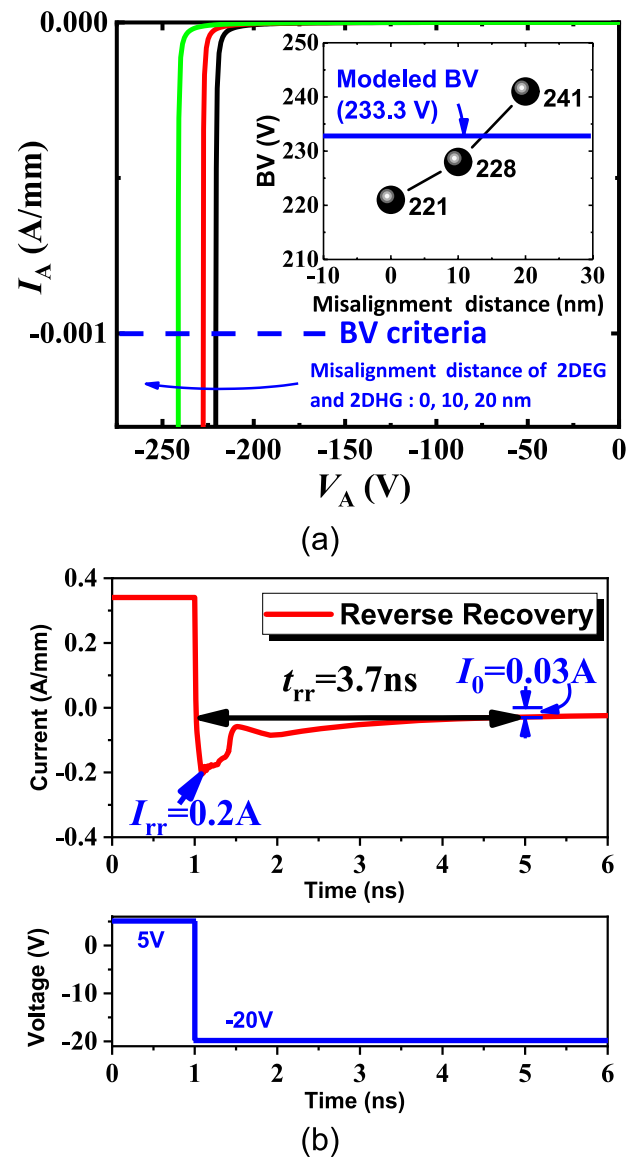

Fig. 9 Simulated **a** breakdown curves and **b** reverse recovery curves of the proposed junction (upper panel) and the voltage pulse wave (lower panel)

this unintentionally neutralized i-type region is that the turn-on voltage may not precisely follow the modeling; on the other hand, this i-type region will enhance the reverse blocking capability of the proposed device architecture, which is a desired advantage.

Another issue is realizing the proposed 2DPD devices through the fabrication process. Although according to the numerical simulation the 2DPD device is resilient to the misalignment errors, growing such misaligned hetero-junctions on the same semiconductor surface may be still challenging. Fortunately, many promising lattice growth techniques have already been explored [38, 39], suggesting

the fabrication of such 2DPD-based devices can be realized in the near future.

4 Conclusion

In this work, we proposed a novel strategy, 2DPD, to realize lateral GaN bipolar devices. The basic theory of the proposed polarization-based junction is established. The essential parameters, such as the turn-on voltage, depletion region width, and the proposed junction's breakdown voltage, are explicitly given. Validated by the calculations and simulations calibrated with experiments, the proposed junction structure shows a good performance in forwarding current, reverse blocking, and reverse recovery. In addition to its compatibility with LED/laser integration, the proposed structure has potential for future electronic applications such as high-power laser sources, portable electrical charging stations, and other power management circuits.

Declarations

Conflict of interest No potential conflicts of interest.

Consent to participate All the authors agree to participate.

Consent for publication All the authors agree to publish.

Ethics approval Not applicable.

Informed consent All people involved in or responsible for the research are informed and consent.

Research involving human participants and/or animals Not applicable.

References

1. Q. Zhao et al., High-power GaN-based vertical light-emitting diodes on 4-inch silicon substrate. Nanomaterials **9**(8), 1–10 (2019). https://doi.org/10.3390/nano9081178
2. M. Zhang, C. Zhao, H. Gong, G. Niu, F. Wang, Porous GaN submicron rods for gas sensor with high sensitivity and excellent stability at high temperature. ACS Appl. Mater. Interfaces **11**(36), 33124–33131 (2019). https://doi.org/10.1021/acsami.9b09769
3. Z. Wang, S. Wang, Y. Yao, A LED-compatible current regulator with integrated electrically adjustable sensor, in *2019 8th International Symposium on Next Generation Electronics, ISNE 2019*, 2019, pp. 1–2. doi: https://doi.org/10.1109/ISNE.2019.8896397.
4. Z. Wang et al., A High-performance tunable LED-compatible current regulator using an integrated voltage nanosensor. IEEE Trans. Electron Dev. **66**(4), 1917–1923 (2019). https://doi.org/10.1109/TED.2019.2899756
5. Z. Wang, Z. Wang, Z. Zhang, D. Yang, Y. Yao, On the Baliga's figure-of-merits (BFOM) enhancement of a novel GaN nanopillar vertical field effect transistor (FET) with 2DEG channel and patterned substrate. Nanoscale Res. Lett. **14**(1), 128 (2019). https://doi.org/10.1186/s11671-019-2960-8
6. C. Florian, F. Mastri, R.P. Paganelli, D. Masotti, A. Costanzo, Theoretical and numerical design of a wireless power transmission link with GaN-based transmitter and adaptive receiver. IEEE Trans. Microw. Theory Tech. **62**(4), 931–946 (2014). https://doi.org/10.1109/TMTT.2014.2303949
7. W. Chen, R.A. Chinga, S. Yoshida, J. Lin, C. Chen, W. Lo, A 25.6 W 13.56 MHz wireless power transfer system with a 94% efficiency GaN Class-E power amplifier, in *2012 IEEE/MTT-S International Microwave Symposium Digest*, 2012, pp. 1–3. doi: https://doi.org/10.1109/MWSYM.2012.6258349.
8. Z. Wang, F. Wang, S. Guo, Z. Wang, Simulation study of high-reverse blocking AlGaN/GaN power rectifier with an integrated lateral composite buffer diode. Micro Nano Lett. **12**(9), 660–663 (2017). https://doi.org/10.1049/mnl.2017.0057
9. F. Wang et al., Simulation design of uniform low turn-on voltage and high reverse blocking AlGaN/GaN power field effect rectifier with trench heterojunction anode. Superlattices Microstruct. **105**, 132–138 (2017). https://doi.org/10.1016/j.spmi.2017.03.029
10. Z. Zheng et al., Gallium nitride-based complementary logic integrated circuits. Nat. Electron. **4**(8), 595–603 (2021). https://doi.org/10.1038/s41928-021-00611-y
11. M. Xiao et al., Lateral p-GaN/2DEG junction diodes by selective-area p-GaN trench-filling-regrowth in AlGaN/GaN. Appl. Phys. Lett. (2020). https://doi.org/10.1063/1.5139906
12. H. Kagel, H. Jacobs, F.F. Bier, J. Glökler, M. Frohme, A novel microtiter plate format high power open source LED array. Photonics (2019). https://doi.org/10.3390/photonics6010017
13. W.Y. Fu, H.W. Choi, GaN PNP light-emitting bipolar junction transistor. J. Phys. D Appl. Phys. **55**(1), 015101 (2022). https://doi.org/10.1088/1361-6463/ac296b
14. Z. Wang, C. Chen, S. Wang, L. Li, Y. Yao, A novel high-performance bipolar GaN diode realized by broadened quantum well and three-dimensional carrier sea, in *2020 IEEE 15th International Conference on Solid-State and Integrated Circuit Technology, ICSICT 2020 - Proceedings*, 2020, pp. 1–3. doi: https://doi.org/10.1109/ICSICT49897.2020.9278234.

15. A. Mase, Y. Nikai, Y. Iida, T. Egawa, M. Miyoshi, Simulation study on novel GaN-based n−p−n heterojunction bipolar transistors with a quaternary AlGaInN emitter and a two-dimensionally conductive base. Phys. Status Sol. (2021). https://doi.org/10.1002/pssa.202100397

16. P. Zuo et al., p−n junction rectifying characteristics of purely n-type GaN-based structures. Phys. Rev. Appl. **8**(2), 024005 (2017). https://doi.org/10.1103/PhysRevApplied.8.024005

17. F. Wang et al., Simulation study of an ultralow switching loss p-GaN gate HEMT with dynamic charge storage mechanism. IEEE Trans. Electron Dev. **68**(1), 175–183 (2021). https://doi.org/10.1109/TED.2020.3036325

18. Y.-T. Shi et al., Property manipulation through pulsed laser annealing in high dose Mg-implanted GaN. J. Appl. Phys. **128**(23), 235704 (2020). https://doi.org/10.1063/5.0028760

19. W. Li et al., Realization of GaN PolarMOS using selective-area regrowth by MBE and its breakdown mechanisms. Jpn. J. Appl. Phys. (2019). https://doi.org/10.7567/1347-4065/ab0f1b

20. C. Liu, Y. Cai, H. Jiang, K.M. Lau, Monolithic integration of III-nitride voltage-controlled light emitters with dual-wavelength photodiodes by selective-area epitaxy. Opt. Lett. **43**(14), 3401 (2018). https://doi.org/10.1364/ol.43.003401

21. K.H. Li, W.Y. Fu, H.W. Choi, Chip-scale GaN integration. Prog. Quantum Electron. **70**, 100247 (2020). https://doi.org/10.1016/j.pquantelec.2020.100247

22. P.P. Maiti et al., Experimental and simulation study of charge transport mechanism in HfTiOx high-k gate dielectric on SiGe heterolayers. Bull. Mater. Sci. **45**(1), 39 (2022). https://doi.org/10.1007/s12034-021-02622-z

23. M. Mishra, N.K. Bhalla, A. Dash, G. Gupta, Nanostructured GaN and AlGaN/GaN heterostructure for catalyst-free low-temperature CO sensing. Appl. Surf. Sci. **481**, 379–384 (2019). https://doi.org/10.1016/j.apsusc.2019.03.125

24. A. Dash et al., Influence of current conduction paths and native defects on gas sensing properties of polar and non-polar GaN. J. Alloys Compd. **898**, 162808 (2022). https://doi.org/10.1016/j.jallcom.2021.162808

25. O. Ambacher et al., Pyroelectric properties of Al (In) GaN/GaN hetero- and quantum well structures. J. Phys. Condens. Matter **14**, 3399–3434 (2002). https://doi.org/10.1088/0953-8984/14/13/302

26. R. Chaudhuri, S.J. Bader, Z. Chen, D.A. Muller, H.G. Xing, D. Jena, A polarization-induced 2D hole gas in undoped gallium nitride quantum wells. Science **365**(6460), 1454–1457 (2019). https://doi.org/10.1126/science.aau8623

27. F. Wang et al., Charge storage impact on input capacitance in p-GaN gate AlGaN/GaN power high-electron-mobility transistors. J. Phys. D Appl. Phys. (2020). https://doi.org/10.1088/1361-6463/ab86e7

28. F. Wang, W. Chen, R. Sun, Z. Wang, Q. Zhou, B. Zhang, An analytical model on the gate control capability in p-GaN Gate AlGaN/GaN high-electron-mobility transistors considering buffer acceptor traps. J. Phys. D Appl. Phys. **54**(9), 095107 (2021). https://doi.org/10.1088/1361-6463/abc504

29. U.K. Mishra, P. Parikh, Y.F. Wu, AlGaN/GaN HEMTs—an overview of device operation and applications. Proc. IEEE **90**(6), 1022–1031 (2002). https://doi.org/10.1109/JPROC.2002.1021567

30. G. Longobardi et al., Impact of donor traps on the 2DEG and electrical behavior of AlGaN/GaN MISFETs. IEEE Electron Dev. Lett. **35**(1), 27–29 (2014). https://doi.org/10.1109/LED.2013.2290471

31. S.M. Sze, K.K. Ng, *Physics of semiconductor devices*, 3rd edn. (2006), 832 p. https://www.wiley.com/en-us/Physics+of+Semiconductor+Devices%2C+3rd+Edition-p-9780470068328

32. P. Mulligan, J. Wang, L. Cao, Evaluation of freestanding GaN as an alpha and neutron detector. Nucl. Instrum. Methods Phys. Res. Sect. A **719**, 13–16 (2013). https://doi.org/10.1016/j.nima.2013.04.019

33. J.Y. Tsao et al., Ultrawide-bandgap semiconductors: research opportunities and challenges. Adv. Electron. Mater. **4**(1), 1600501 (2018). https://doi.org/10.1002/aelm.201600501

34. Z. Wang et al., Proposal of a novel enhancement type AlGaN/GaN HEMT using recess-free field coupled gate. Superlattices Microstruct. **122**(July), 343–348 (2018). https://doi.org/10.1016/j.spmi.2018.07.016

35. O. Hilt, F. Brunner, E. Cho, A. Knauer, E. Bahat-Treidel, J. Wurfl, Normally-off high-voltage p-GaN gate GaN HFET with carbon-doped buffer. Proc. Int. Symp. Power Semicond. Dev. ICs **50**, 239–242 (2011). https://doi.org/10.1109/ISPSD.2011.5890835

36. Inc. Silvaco, *Atlas User's Manual*. 2016. https://dynamic.silvaco.com/dynamicweb/jsp/downloads/DownloadManualsAction.do?req=silen-manuals&name=atlas. Accessed May 2016

37. L. Nela, G. Kampitsis, J. Ma, E. Matioli, Fast-switching tri-anode schottky barrier diodes for monolithically integrated GaN-on-Si power circuits. IEEE Electron Dev. Lett. **41**(1), 99–102 (2020). https://doi.org/10.1109/LED.2019.2957700

38. J. Fricke et al., Patterned growth on GaAs (311)A substrates: engineering of growth selectivity for lateral semiconductor nanostructures. J. Appl. Phys. **86**(5), 2896–2900 (1999). https://doi.org/10.1063/1.371138

39. A. Madhukar, Growth of semiconductor heterostructures on patterned substrates: defect reduction and nanostructures. Thin Solid Films **231**(1–2), 8–42 (1993). https://doi.org/10.1016/0040-6090(93)90701-P